remote sensing

MDPI

Article

Compounding Effects of ENSO and PDO on Coastal Chlorophyll-A over the Southern Luzon Strait During Boreal Winters in the Early 2020s

Yu-Hao Tseng [1], Chung-Ru Ho [1,*], Haonan Chen [2] and Liping Wang [2]

[1] Department of Marine Environmental Informatics, National Taiwan Ocean University, Keelung 202301, Taiwan; 21281001@email.ntou.edu.tw
[2] Department of Electrical and Computer Engineering, Colorado State University, Fort Collins, CO 80523, USA; haonan.chen@colostate.edu (H.C.); liping.wang@colostate.edu (L.W.)
* Correspondence: b0211@mail.ntou.edu.tw

Highlights

What are the main findings?

- The compounding effects of a cold-phase PDO and ENSO dually modulated regional hydrology, driving extreme riverine discharge during the 2020–21 La Niña while buffering against drought during the 2023–24 El Niño.
- Coastal chlorophyll-a blooms were fueled by precipitation-inferred terrestrial runoff and monsoon-driven upwelling, with their seaward dispersion into the northern South China Sea actively regulated by the climate-modulated Kuroshio intrusion.

What are the implications of the main findings?

- Accurately projecting coastal biogeochemical responses to climate anomalies requires an integrated approach that couples oceanic dynamics with terrestrial hydrological forcing.
- This study provides a predictive structure to assess marine ecosystem resilience in dynamic coastal boundaries where a high-sea-level western boundary current directly intersects a low-sea-level estuary.

Abstract

The coastal ocean off northern Luzon Island (NLC, 18.25°N–18.75°N, 121°E–122.25°E) is strongly influenced by atmospheric forcing, terrestrial runoff, and Kuroshio intrusion (KI). We investigate contrasting winter (November–January or NDJ) hydrographic and biogeochemical responses during the 2020–21 La Niña and 2023–24 El Niño under a persistent cold-phase Pacific Decadal Oscillation (PDO). During NDJ 2020–21, precipitation over the Cagayan River basin increased by ~8 mm day^{-1}. In contrast, the cold PDO substantially moderated the El Niño-induced precipitation reduction during NDJ 2023–24, resulting in an anomaly of approximately −3 mm day^{-1}. Coastal chlorophyll-a (Chl-a) anomalies were +0.28 ± 0.22 and −0.04 ± 0.10 mg m^{-3} during the two winters, respectively. Concurrently, geostrophic observations revealed weaker KI in December 2020 and stronger KI in December 2023 relative to the cold PDO background. The weaker KI reduced offshore export and favored Chl-a accumulation near northern Luzon, whereas stronger KI enhanced westward advection toward the South China Sea (SCS). Our results demonstrate that ENSO-dominated, PDO-modulated processes mediated by the atmosphere and Kuroshio regulate coastal nutrient supply, linking precipitation-inferred

Academic Editors: Hatim Sharif and Gabriel Navarro

Received: 8 October 2026
Revised: 20 November 2026
Accepted: 27 November 2026
Published: 29 November 2026

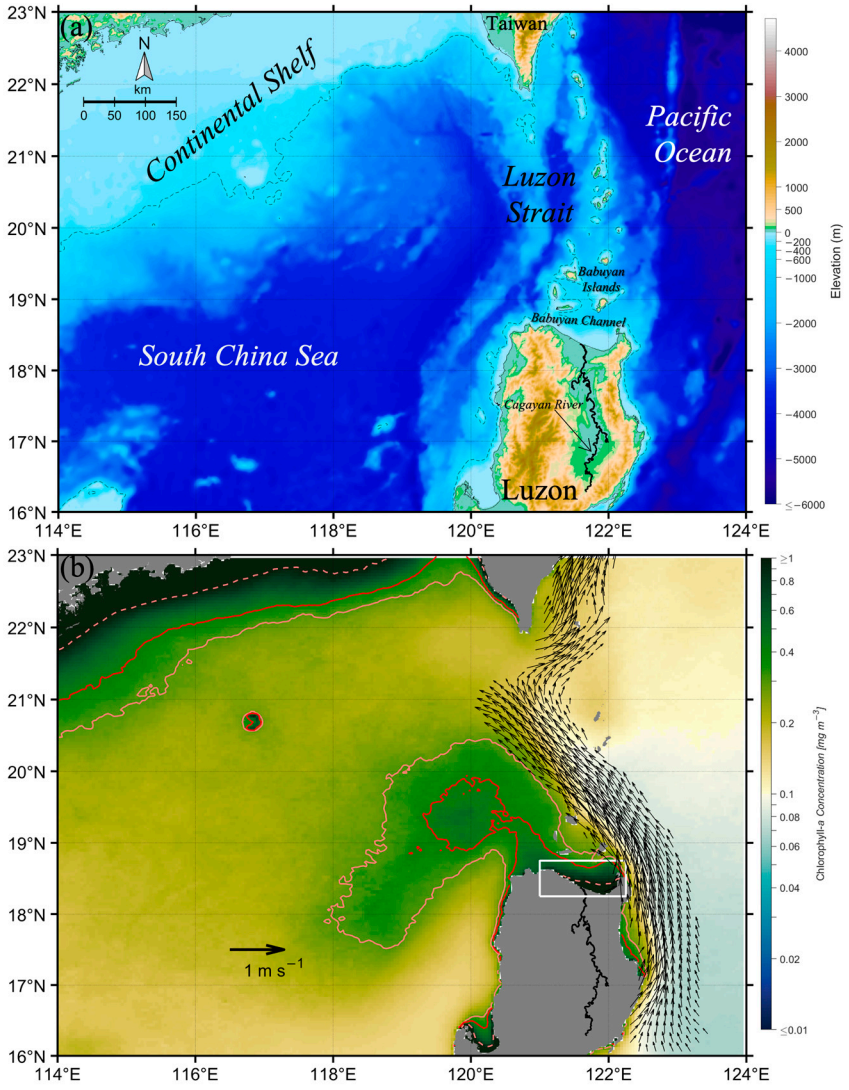
Copyright: © 2026 by the authors. Licensee MDPI, Basel, Switzerland. This article is an open access article distributed under the terms and conditions of the Creative Commons Attribution (CC BY) license.

terrestrial runoff, coastal productivity, and nutrient-poor Kuroshio waters to biogeochemical variability in the northern SCS.

Keywords: Pacific Decadal Oscillation (PDO); El Niño-Southern Oscillation (ENSO); precipitation; sea surface chlorophyll-a; Luzon Strait; Kuroshio

1. Introduction

The Luzon Strait (LS, 18.25°N–21°N, 121.25°E–122.25°E), a critical passage between Taiwan and Luzon Island (Figure 1a), is a dynamic interface where the Kuroshio intrusion (KI) enters the northern South China Sea (SCS) during winter [1,2]. This region features complex physical and biogeochemical interactions. The Kuroshio transports warm, saline, and oligotrophic waters northward from the tropical western Pacific Ocean (Figure 1b). During winter, when the Kuroshio intrudes into the LS with a relatively high sea level anomaly (SLA), this western Pacific water mass is propelled through an El Niño–Southern Oscillation (ENSO)-related low SLA off northwestern Luzon (NWL-SLA) [3]. Concurrently, the northeast monsoon induces a positive wind stress curl (WSC) off northwestern Luzon, driving regional Ekman pumping. This process generates a cyclonic gyre and a localized low SLA, which further enhances coastal upwelling and nutrient enrichment along the coast [3–6].



https://doi.org/10.3390/rs18234141

Figure 1. (**a**) The study area near the Luzon Strait. The shading colors represent terrestrial elevation and ocean depth. The black line on Luzon Island and the dashed contours denote the CR and 500-m depth, respectively. (**b**) The mean state of monthly GlobColour Chl-a in December near the region of the Luzon Strait from 2000 to 2024 (unit: mg m^{-3}). The black vector group is the absolute dynamic topography (ADT)-derived Kuroshio main path in December from 1993 to 2024 (unit: m s^{-1}). The white solid box indicates the spatial domain of the NLC. The pink dashed, red solid, and pink solid lines denote GlobColour Chl-a contours of 1, 0.4, and 0.3 mg m^{-3}, respectively.

The regional marine ecosystem is highly susceptible to basin-scale interannual and interdecadal climate variability, driven primarily by ENSO and the Pacific Decadal Oscillation (PDO). Individually, these climate oscillations modulate Pacific Ocean currents [7], precipitation patterns, and marine productivity [8,9]. In the LS, the Kuroshio dynamics are governed by a combination of oceanic factors (e.g., mesoscale eddies and the North Equatorial Current bifurcation latitude, NECBL), wind stress, and topography [10–12]. During El Niño/La Niña or warm/cold PDO phases, northward/southward shifts of the NECBL [13] often weaken/strengthen the Kuroshio transport east of the Philippines. This, in turn, enhances/weakens its intrusion into the SCS via the "teapot effect" [14–20]. The intensity of oligotrophic water intrusion establishes a robust geostrophic response to the ENSO and the PDO over the NWL-SLA [3]. Dynamically, this El Niño-related low SLA facilitates Kuroshio-driven offshore transport of sea surface chlorophyll-a (Chl-a), carrying nutrient-rich waters from the coastal ocean off northern Luzon Island (NLC; 18.25°N–18.75°N, 121°E–122.25°E) into the northeastern SCS. This process significantly alters the regional marine ecosystem [2,12,14,21] and nutrient budgets [22,23].

In addition to ocean dynamics, these large-scale climate oscillations systematically govern precipitation-inferred terrestrial nutrient inputs from the Cagayan River (CR) basin, the largest river basin in the Philippines with a drainage area of 27,281 km^2 [24], into the NLC via the Babuyan Channel (Figure 1a). Individually, the ENSO significantly regulates precipitation patterns across the northwest Pacific [25] through the anomalous western North Pacific anticyclone (WNPAC) over the Philippine Sea [26]. This modulation strongly affects tropical cyclone activity [27–29] over regions where complex topography creates highly localized precipitation variability [30–36], and is ultimately inferred to modulate riverine nutrient discharge from the CR catchment. Concurrently, the PDO establishes the decadal background state, modulating the KI via anomalous WSC. The KI subsequently acts as a lateral biophysical conveyor, regulating coastal Chl-a dispersion. During a warm-phase PDO or El Niño, reduced regional precipitation diminishes riverine nutrient fluxes [37], whereas the opposite occurs during a cold-phase PDO or La Niña.

While the individual impacts of the ENSO and the PDO are well documented, previous studies on their compounding effects [38–40] have primarily focused on local diurnal convection over Borneo [41], the Maritime Continent [42], Taiwan [43,44], and Luzon [45]. The LS represents a major climatological boundary, characterized by a distinct meridional dipole in both atmospheric and hydrological responses [46], as reflected in the long-term mean 850-hPa wind and geopotential height fields [47]. Broadly, the dominant mode of spring precipitation variability over East Asia features a prominent southern China–Southeast Asia dipole [48]. During El Niño winters, the anomalous WNPAC spanning the SCS and the Philippine Sea drives persistent anomalous subsidence and low-level moisture divergence over Luzon Island [26,30,37,45], while simultaneously enhancing moisture convergence and precipitation over subtropical southern China [37,48]. Regionally, a similar meridional contrast is evident across Luzon Island, where long-term trends in monsoon rainfall and extreme precipitation events exhibit a north-south dipole, with drying in the north and wet in the south [37,47,49]. Their frameworks treat oceanic and atmospheric forcing in isolation. Consequently, how the aforementioned climate modes

jointly affect the unique land–ocean–atmosphere nutrient system in the NLC remains largely unexplored.

To address this critical research gap, this study proposes an "ENSO-dominated, PDO-modulated" analytical framework. Previously, elucidating this interdisciplinary chain of processes was challenging because the coarse spatial resolution of observational datasets limited their ability to resolve mesoscale and submesoscale dynamics in the topographically complex LS and surrounding island region. However, recent advances in satellite remote sensing, including resolution-improved absolute dynamic topography (ADT) to resolve geostrophic currents, gap-free ocean color sensors for Chl-a, and an innovative observation-based precipitation product, provide an unprecedented capability to observe these processes comprehensively (Figure 1b). Tracing how large-scale climate forcing cascades down to regional physical-biogeochemical coupling is crucial for predicting the resilience of coastal marine environments under compounding, multi-scale climate scenarios [50–52]. Compared with existing compound-event-related studies, our proposed framework explicitly distinguishes the temporal and physical roles of overlapping climate modes. We hypothesize that the interannual ENSO variability dominates hydrological and meteorological anomalies, while the persistent decadal cold-PDO modulates these responses and the KI through constructive or destructive phase interference.

Focusing on the early 2020s, a period marked by a record-breaking, persistent cold-phase PDO regime (cold-PDO) beginning in March 2020 and continuing to the present (Figure 2), this study investigates the compounding effects of this decadal background of cold-PDO coupled with distinct ENSO phases, specifically the 2020–21 La Niña and the 2023–24 El Niño winters. By evaluating the physical chain linking regional precipitation, local WSC, and the intensity of the KI, this study elucidates how ENSO-PDO phase transitions govern Chl-a in the NLC, and how varying KI patterns regulate the subsequent offshore distribution of Chl-a during the 2020–21 and 2023–24 winters. Ultimately, this study advances our understanding of the resilience of coastal marine ecosystems under compounding climate forcing.

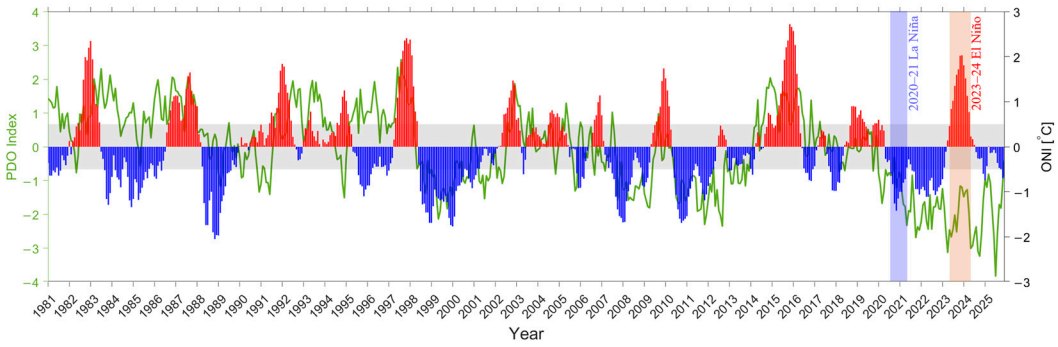


Figure 2. Time series of the monthly PDO index (green solid line) and the Oceanic Niño Index (ONI, blue and red bars) (unit: °C) from 1981 to 2024. The gray shaded area denotes the below-threshold value (≤|0.5|) of the ONI and PDO, respectively. The blue- and red-shaded areas illustrate the 2020–21 La Niña and 2023–24 El Niño events, respectively. The official data are available at https://www.ncei.noaa.gov/pub/data/cmb/ersst/v5/v6/index/ersst.v6.pdo.dat (accessed on 7 October 2026) for the PDO and https://www.cpc.ncep.noaa.gov/products/analysis_monitoring/enso/oni/v6/ (accessed on 7 October 2026) for the ONI.

2. Materials and Methods

2.1. Materials

2.1.1. Topography and River Distribution

The topographical data used to delineate oceanic and terrestrial features were obtained from the ETOPO1 1 Arc-Minute Global Relief Model provided by the National Oceanic and Atmospheric Administration (NOAA) National Geophysical Data Center (https://doi.org/10.7289/V5C8276M). To identify the distribution of precipitation-inferred riverine nutrient outflows into the NLC, we utilized the ASTER Global Water Bodies Database V001 provided by the National Aeronautics and Space Administration (NASA) Land Processes Distributed Active Archive Center (https://doi.org/10.5067/ASTER/ASTWBD.001). The Cagayan River, depicted by the black line on Luzon Island in Figure 1a, acts as the region's primary source of terrestrial freshwater and nutrient inputs.

2.1.2. SLA, ADT, and Ocean Currents

SLA and ADT data were acquired from the Copernicus Marine Environment Monitoring Service (CMEMS; SEALEVEL_GLO_PHY_L4_MY_008_047 product, downloaded in March 2025) at https://doi.org/10.48670/moi-00148. We derived surface geostrophic currents directly from the ADT fields using standard geostrophic balance. We used the latest available data versions, providing daily coverage at a refined spatial resolution of 0.125° × 0.125° over 1993–2024. This doubled spatial resolution, compared to previous versions, significantly improves the ability to resolve mesoscale and coastal currents around the topographically complex islands in the LS. To clearly decompose the currents into wind-induced and geostrophic components and identify the KI, daily 0.25° × 0.25° surface Ekman and geostrophic current data were obtained from the CMEMS Global Total (COPERNICUS-GLOBCURRENT) currents product (https://doi.org/10.48670/mds-00327, accessed in March 2025).

2.1.3. Winds

Monthly winds at 10-m height, 850-hPa geopotential height, and 850-hPa wind were obtained from the fifth-generation European Centre for Medium-Range Weather Forecasts (ECMWF) reanalysis (ERA5; https://cds.climate.copernicus.eu/datasets, accessed in March 2025); 10-m wind speed fields characterize near-surface atmospheric conditions. Basin-scale geopotential height and 850-hPa wind characterize the atmospheric background over land and ocean.

2.1.4. Chl-a

Monthly Level-4 (L4) Chl-a concentrations from September 1997 to 2024 were obtained from the Copernicus-GlobColour Bio-Geo-Chemical L4 product (https://doi.org/10.48670/moi-00281, product identification: OCEANCOLOUR_GLO_BGC_L4_MY_009_104). This dataset merges optical sensor data from the Seaviewing Wide Field-of-view Sensor (SeaWiFS, since September 1997), the Moderate Resolution Imaging Spectroradiometer (MODIS, since February 2000), the Medium Resolution Imaging Spectrometer (MERIS, since February 2002), Visible Infrared Imaging Radiometer Suite aboard Suomi National Polar-orbiting Partnership (VIIRS-SNPP, since 2012), and Visible Infrared Imaging Radiometer Suite aboard Joint Polar Satellite System-1 (VIIRS-JPSS1, since 2018) to address observation gaps. This gap-free blended product eliminates biases from missing observations in specific months while maintaining 4-km spatial and monthly temporal resolutions.

2.1.5. Climate Indices

Large-scale climate variability was represented using two primary indices. The ENSO state was determined using the Oceanic Niño Index (ONI) from the NOAA Climate Prediction Center (CPC), with El Niño (La Niña) events defined as ONI values exceeding 0.5 (or falling below −0.5). Interdecadal climate variability was assessed using the Pacific Decadal Oscillation (PDO) index [53] from NOAA's National Centers for Environmental Information (NCEI), based on the ERSST V6 dataset at https://www.ncei.noaa.gov/access/monitoring/pdo/ (accessed in March 2025).

2.1.6. Meteorological Data

To evaluate regional precipitation anomalies and hydrological forcing over the Cagayan River basin, this study integrates three complementary satellite-derived rainfall products at their native resolutions. Historical baselines and decadal shifts in monsoon precipitation over the Philippine Sea and Luzon are characterized using the monthly 0.25° × 0.25° NASA Tropical Rainfall Measuring Mission (TRMM) 3B42 dataset, which serves as a valuable long-term climate benchmark [26,30,47]. For contemporary, high-resolution analyses, we employ the 0.1° × 0.1° NASA Integrated Multi-satellitE Retrievals for Global Precipitation Measurement (GPM) mission (IMERG) "Final Run" product. By incorporating monthly rain-gauge calibrations to correct systematic biases, IMERG's native 0.1° grid provides the high-fidelity spatial estimates necessary to resolve both large-scale East Asian and island-scale diurnal rainfall variations over Luzon's complex terrain [45,48].

Additionally, localized orographic rainfall and extreme events over the rugged topography of northern Luzon are resolved using the Climate Hazards Group InfraRed Precipitation with Station data (CHIRPS) dataset V3.0, developed by the Climate Hazards Center (CHC) at the University of California, Santa Barbara (UCSB). By blending satellite infrared observations with dense in situ station records, CHIRPS delivers daily rainfall estimates at its native, ultra-fine 0.05° × 0.05° (~5 km) resolution. This high-resolution dataset exhibits low systematic bias, offering exceptional event detectability over the Cagayan River basin [49].

To reconcile the differing temporal coverage and spatial resolutions of these datasets, this study adopts two temporal frameworks designed to optimize both climatological robustness and process-oriented precision. To capture low-frequency climate variability, including the decadal modulation associated with the PDO, we established a continuous 44-year climatology (1981–2024) using the long-term CHIRPS dataset, exceeding the World Meteorological Organization (WMO)-recommended 30-year baseline period. ERA5 850-hPa data covering the same period were subsequently used to characterize the background atmospheric conditions. However, the geostrophic data and Chl-a are restricted to post-1993 and post-1997 eras, respectively. This restriction ensures rigorous observational consistency by utilizing currents, winds, and gap-free Chl-a data from CMEMS (available since 1993), ERA5 (following CMEMS), and GlobColour (available since September 1997), respectively. Because this study calculates anomalies as the deviation of a specific event from its respective long-term mean, these different baselines help isolate interannual extremes within the decadal background without cross-contaminating the datasets.

2.2. Methods

2.2.1. Composite Analysis

We performed composite analysis to isolate and quantify the distinct impacts of large-scale climate variability on Chl-a distributions and regional hydrodynamics along the NLC. Based on the PDO and ONI time series for 1981–2024 (Figure 2), monthly records

were classified according to the positive (warm) and negative (cold) phases of each climate mode, yielding four combinations: warm PDO–El Niño, warm PDO–La Niña, cold PDO–La Niña, and cold PDO–El Niño. Monthly Chl-a and associated physical parameters, including geostrophic currents and wind anomalies, were then composited for each combination. This approach reduces short-term noise and highlights differences in the regional biogeochemical and physical ocean states under contrasting climate conditions, thereby providing insights into the combined effects of the PDO and the ENSO. In the subsequent composite figures, N denotes the number of specific climate combination events (months) included in each average.

To quantify the statistical significance of the spatial composite fields and distinguish climate-driven signals from internal variability, a two-tailed Student's *t*-test was conducted on the datasets. Recognizing that composite samples from specific PDO-modulated ENSO events may exhibit temporal autocorrelation, the test was implemented to evaluate significance at a 95% confidence level (*p*-value, hereafter $p < 0.05$). To effectively communicate these robust quantitative results without introducing the visual clutter associated with conventional stippling or dense vectors, a non-significant masking technique was applied to the final map. Consequently, in the subsequent composite maps, only the grids that strictly satisfy this 95% significance criterion are highlighted with color shading, whereas the statistically insignificant grids remain deliberately uncolored. This approach explicitly addresses uncertainties in sample size and ensures that the visualized spatial patterns represent systematic, statistically robust physical responses.

2.2.2. Coordinate Transformation

The KI pattern is primarily oriented westward between 90° and 270° in the Cartesian coordinate system, where east is 0° and angles increase counterclockwise. To quantify the KI intensity along its preferred streaming direction, we projected the current velocity vectors from the original axes (x1, y1) onto the principal flow (along-stream) axes (x2, y2). The original coordinate system for the current field (u_c, v_c), denoted by x1 for eastward and y1 for northward components, is rotated in a counterclockwise direction from the (x1, y1) to the along-stream *x*-axis (x2) and the cross-stream *y*-axis (y2) by the principal axis angle θ (0° at east). The x2 and its direction are chosen to be parallel to and the same as the long-term mean current direction of the KI in December ($\mathbf{V_c}$). The $\mathbf{V_c}$ is driven from the long-term mean currents ($\overline{u_c}$, $\overline{v_c}$) in axes (x1, y1), expressed as $\mathbf{V_c} = \overline{u_c}\,\mathbf{i} + \overline{v_c}\mathbf{j}$. The $\overline{u_c}$ is the mean zonal velocity, and the $\overline{v_c}$ is the mean meridional velocity of the current fields in the Kuroshio branch, whose vector magnitudes were greater than the Kuroshio branch's spatial median. After θ is calculated by $\theta = \tan^{-1}(\frac{\overline{v_c}}{\overline{u_c}})$, the rotated velocity components (u_c, v_c) projected to (u'_c, v'_c) can be calculated as:

$$\begin{cases} u'_c = u_c \cdot cos\theta + v_c \cdot sin\theta \\ v'_c = -u_c \cdot sin\theta + v_c \cdot cos\theta \end{cases}, \quad (1)$$

where u'_c and v'_c represent the along-stream and cross-stream velocity, respectively, for the rotated coordinate system. This rotated coordinate system ($\theta = \theta_c$), based on the December mean state of the KI, can interpret and quantify the deflection of the Kuroshio branch each year. By restricting the baseline strictly to the December climatology, the mean flow in the selected region is physically constrained to a specific directional envelope, predominantly westward/northwestward into the SCS. Consequently, the long-term mean velocity components ($\overline{u_c}$, $\overline{v_c}$) used to calculate θ do not cross into symmetrical or opposing quadrants, ensuring that the standard inverse tangent calculation robustly preserves the physical directionality without quadrant ambiguity. This study will use u'_c to quantify the intensity of the KI and apply the same method to quantify the intensity of the northeast monsoon (u'_w) from original westerlies (u_w) and southerlies (v_w) with ($\theta = \theta_w$).

Additionally, to quantify the Ekman pumping effect driven by the northeast monsoon, the WSC is derived from the ERA5 10-m wind fields. The surface wind stress ($\boldsymbol{\tau}$) is first calculated using the bulk formula:

$$\boldsymbol{\tau} = (\tau_x,\ \tau_y) = \rho_a \cdot C_d \cdot U_{10} \cdot (u_w,\ v_w)\ , \quad (2)$$

where ρ_a is the density of air at the surface (1.25 kg m^{-3}), C_d is the wind drag coefficient (1.5×10^{-3}), and U_{10} is the 10-m wind speed, $\sqrt{{u_w}^2 + {v_w}^2}$. τ_x and τ_y represent the zonal and meridional components of the wind stress, respectively. Subsequently, the WSC is computed as:

$$\mathrm{WSC} = (\boldsymbol{\nabla} \times \boldsymbol{\tau})_z = \frac{\partial \tau_y}{\partial x} - \frac{\partial \tau_x}{\partial y}\ . \quad (3)$$

3. Results

3.1. Cagayan River Catchment Precipitation

We propose that precipitation serves as the primary physical bridge linking the ENSO and cold-PDO to NLC Chl-a variability. Monthly mean precipitation from 1981 to 2024, based on the CHIRPS product, shows variations across the CR catchment (P_{CR}; Figure 3a). The zonal-mean P_{CR} from upstream of 16°N to downstream of 18.5°N, shown in Figure 3b, decreased markedly during the positive phases of the ONI and PDO (red lines) relative to their negative ones (blue lines), with reductions exceeding 5 and 2 mm day^{-1}, respectively, and being particularly pronounced upstream. The 13-month running-mean P_{CR} time-latitude Hovmöller diagram (Figure 3c) further reveals that this climate-related precipitation variability extends across the entire CR catchment [54]. Notably, the 13-month running average of accumulated P_{CR} shows a negative correlation with the ONI, with a correlation coefficient (r) = −0.52 ($p < 0.01$) (Figure 3d).

A comparison of three precipitation products, including TRMM, GPM IMERG, and CHIRPS, shows a high correlation ($r \geq 0.83$; $p < 0.01$) among their monthly values (Figure 4a). To evaluate the regional hydrometeorological anomalies over Luzon, this study diagnostically evaluates the monthly-mean precipitation rate (unit: mm day^{-1}) in the CR basin to resolve how cross-time-scale climate conditions modulate regional rainfall anomalies of recent El Niño and La Niña events, 2020–21 and 2023–24 winters, during the cold-PDO (Figure 4b).

Relative to the 1981–2024 NDJ climatology (Figure 5), Figure 6a illustrates the 850-hPa geopotential height and wind anomalies during NDJ 2020–21. The concurrent occurrence of La Niña and a persistent cold-PDO resulted in constructive atmospheric interference, substantially weakening the WNPAC and confining its influence to a more restricted region. This circulation response was associated with enhanced zonal sea surface temperature (SST) anomaly gradients over the Philippine Sea and intensified Walker circulation [13,29,45]. Meanwhile, La Niña favored the development of a pronounced anomalous cyclone over the Philippine Sea, representing a marked reversal of the regional atmospheric circulation [29]. This anomalous cyclone directly drove the extreme precipitation increases observed over the CR basin (Figure 4b,c).

In contrast, canonical El Niño events typically enhance the WNPAC, placing Luzon under intense anomalous subsidence and low-level moisture divergence [29,47]. Additionally, regional moisture transport from the northeast monsoon was expected to be severely reduced, resulting in an extreme meteorological drought with a pronounced deficit in the monthly-mean precipitation rate [55]. However, during the NDJ 2023–24 El Niño, this conventional expectation was disrupted. The persistent cold-PDO weakened the anomalous high-pressure envelope of the WNPAC during NDJ 2023–24, resulting in destructive interference, even though the 850-hPa geopotential height anomaly was positive

during NDJ 2023–24 (Figure 6c) and in December 2023 (Figure 6d). Consequently, uninhibited moisture transport from the wintertime northeast monsoon likely relieved the El Niño-induced monsoonal drought over the CR basin (Figure 4c) by maintaining near-normal riverine discharge into the NLC.

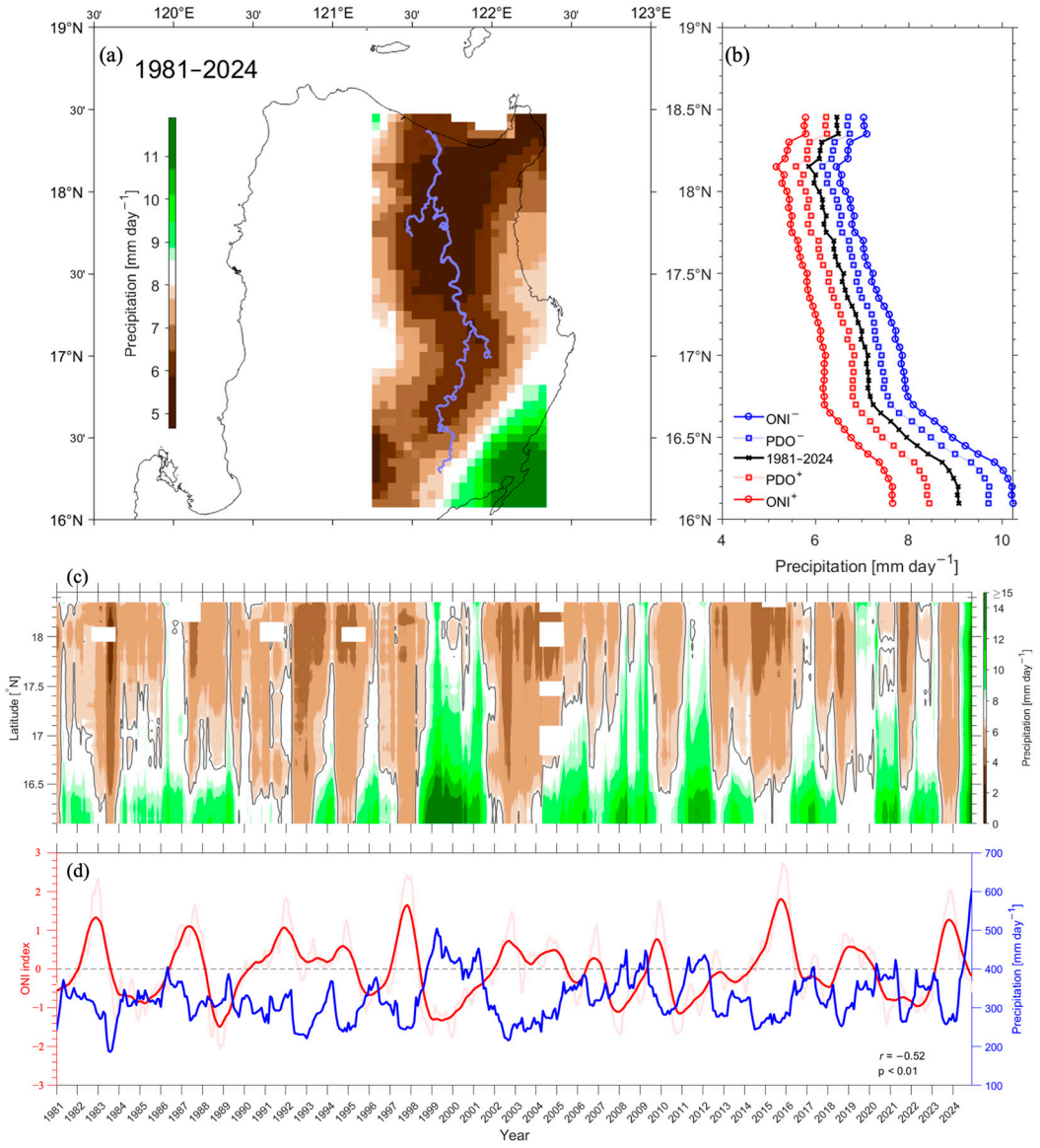


Figure 3. (**a**) The average CHIRPS precipitation in the CR area (P_{CR}; 16°N–18.5°N, 121.25°E–122.25°E) from 1981 to 2024 (unit: mm day^{-1}). (**b**) The zonal average P_{CR} during 1981–2024 (black line), positive PDO index (square-marked light-red line), negative PDO index (square-marked light-blue line), positive ONI (circle-marked red line), and negative ONI (circle-marked blue line). (**c**) The 13-month running average time–latitude plot of zonal average P_{CR}. The black contour denotes 7.5 mm day^{-1}. (**d**) The red and blue lines are the 13-month running mean of the ONI and the accumulated P_{CR}, respectively. Their correlation coefficient (r) is −0.52. The shaded red and blue lines represent the original ONI and accumulated P_{CR}, respectively.

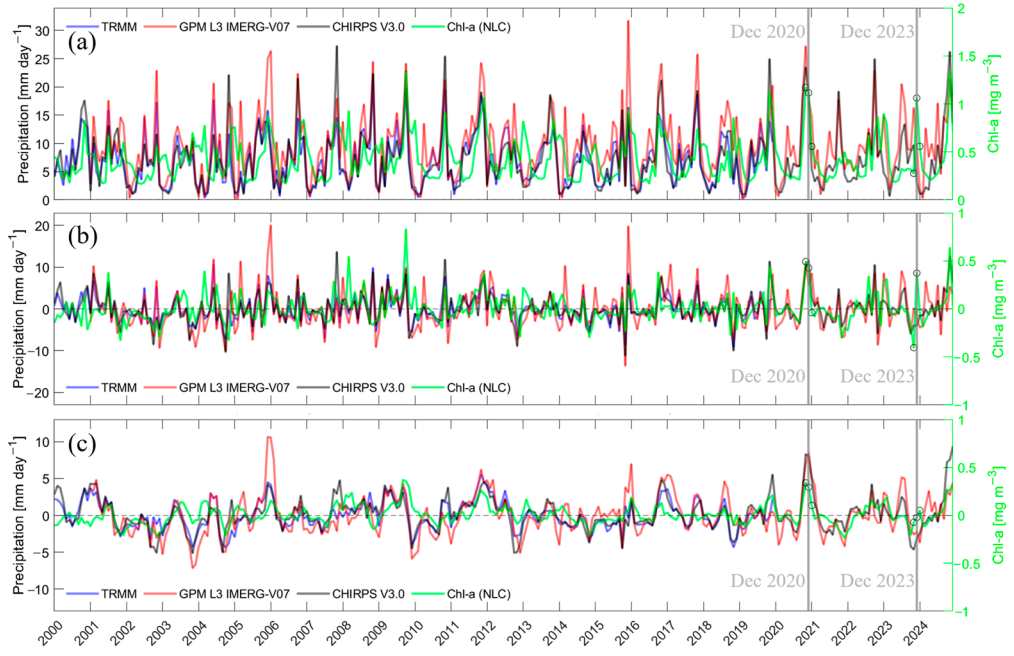


Figure 4. Time series of mean precipitation in the Cagayan River basin (P_{CR}; unit: mm day^{-1}) and the mean Chl-a in the NLC (Chl-a$_{NLC}$; unit: mg m^{-3}) from 2000 to 2024. (**a**,**b**) are their monthly values and monthly anomalies relative to their corresponding monthly climatology spanning different periods as listed in Table 1, respectively. The P_{CR} derived from TRMM, GPM IMERG, CHIRPS, and Chl-a$_{NLC}$ are drawn in blue, red, black, and green solid lines, respectively. (**c**) Same as (**b**), but for their 3-month running averages. Three black circles around the gray lines represent Chl-a$_{NLC}$ in November, December, and January.

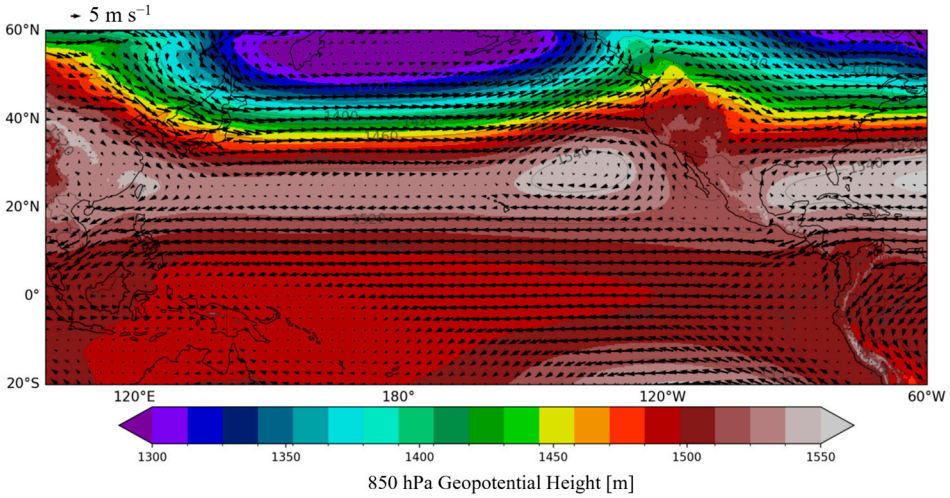


Figure 5. The NDJ climatology of ERA5 850-hPa geopotential height (unit: m) and 850-hPa wind vectors (unit: m s^{-1}) during 1981 to 2024 shows the atmospheric boundary crossing the Pacific Ocean basin departing the Luzon Strait.

Table 1. The monthly anomalies of mean precipitation in the Cagayan River basin (ΔP_{CR}) from three precipitation products (unit: mm day^{-1}) and the monthly anomalies of Chl-a concentration in the NLC (ΔChl-a, unit: mg m^{-3}) with their standard deviations and climatological means. The parentheses indicate the climatology period: December (Dec) or NDJ.

	ΔP_{CR} (TRMM)	**ΔP_{CR} (IMERG)**	**ΔP_{CR} (CHIRPS)**	**ΔChl-a**
Dec 2020	-	+5.85 ± 2.43	+11.57 ± 6.53	+0.42 ± 0.22

NDJ 2020–21	-	+8.46 ± 1.45	+8.04 ± 2.66	+0.28 ± 0.22
Dec 2023	-	−2.41 ± 3.71	−4.06 ± 3.12	+0.37 ± 0.38
NDJ 2023–24	-	−2.22 ± 2.70	−3.21 ± 1.95	−0.04 ± 0.10
Dec Climatology	7.57 (1998–2019)	11.98 (2001–2024)	7.33 (1981–2024)	0.69 (September 1997–2024)
NDJ Climatology	7.60 (1998–2019)	11.48 (2001–2024)	7.90 (1981–2024)	0.66 (September 1997–2024)

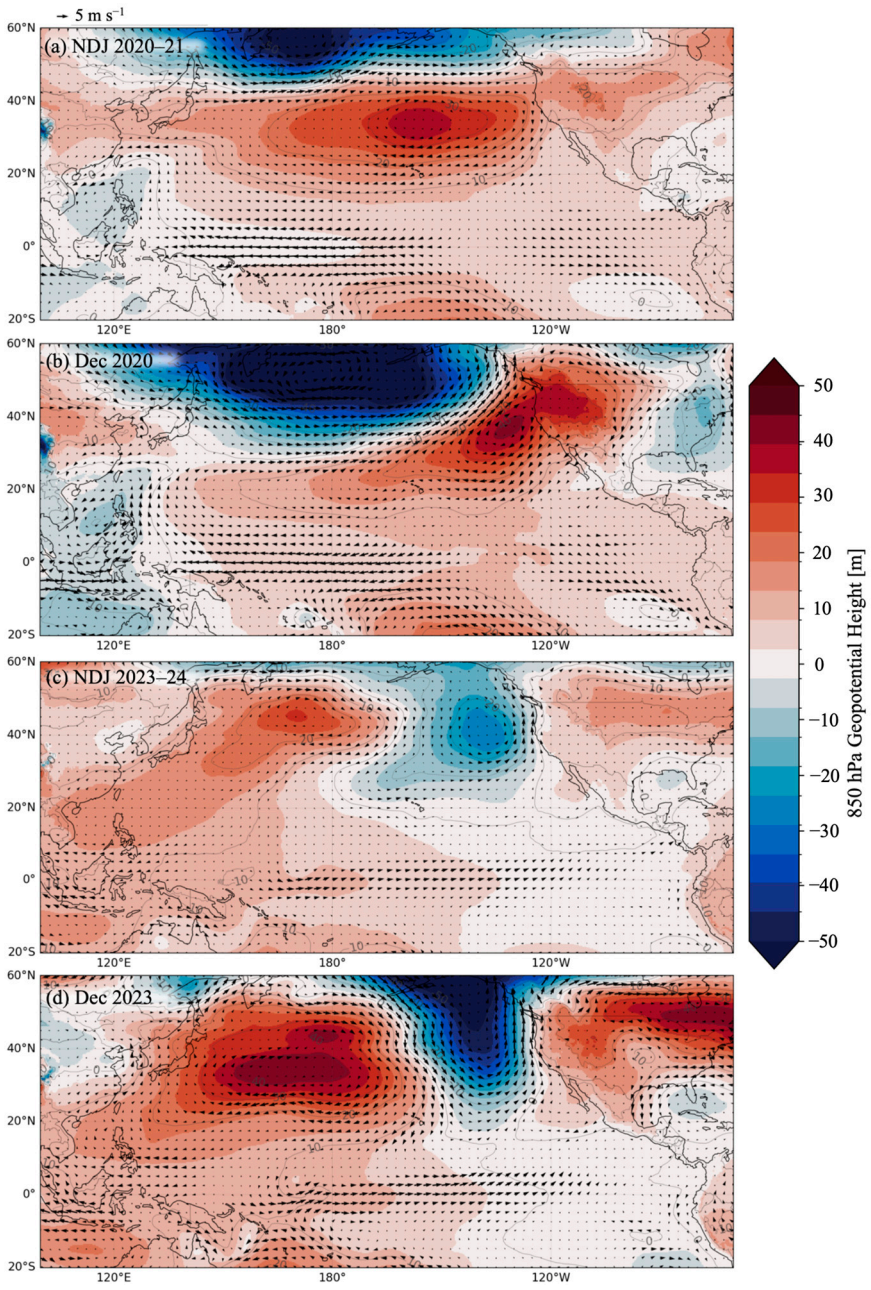


Figure 6. Anomalies of ERA5 850-hPa geopotential height (unit: m) and 850-hPa wind vectors (unit: m s^{-1}) for NDJ (**a**) 2020–21, (**c**) 2023–24, and December (**b**) 2020, (**d**) 2023 in the North Pacific basin with baseline from 1981 to 2024. The anomalies highlight contrasting atmospheric responses under the cold-PDO: an anomalous Philippine Sea cyclone via constructive interference in 2020–21 versus a weakened WNPAC via destructive interference in 2023–24.

3.2. Spatiotemporal Variations of Chl-a in the NLC

To understand the biological consequences of modulated atmospheric and hydrological anomalies over northern Luzon Island, we examine spatiotemporal variations in Chl-a in the NLC and adjacent regions in the northeastern SCS (Figure 1b). Under canonical El Niño conditions, the regional climate is characterized by pronounced droughts across the Philippine archipelago [33,46]. The establishment of the WNPAC induces persistent large-scale atmospheric subsidence and moisture divergence over northern Luzon [47]. This suppression of precipitation severely restricts the hydrological discharge of the Cagayan River. Consequently, the inferred decreases in terrestrial nutrient and dissolved solid inputs typically limit coastal nutrient pools, contributing to a dramatic reduction in coastal phytoplankton biomass and Chl-a during mature El Niño winters.

During winters in a cold-PDO climate background, compared to climatology, the NDJ 2020–21 exhibited anomalous increases in NLC Chl-a, whereas the NDJ 2023–24 exhibited anomalous decreases (Figure 4c). These two Chl-a anomalies were driven by distinct physical-biogeochemical coupling mechanisms operating across different temporal scales. Because the CR behaves as a classic small mountainous river (SMR) characterized by steep slopes and high sediment yields, such extreme synoptic precipitation triggers a rapid, pulse-like hydrologic flushing event [56]. This massive runoff is inferred to have flushed enormous quantities of suspended sediment, wash load, and terrestrial nutrients, including nitrogen and phosphorus, directly into the NLC [24,57].

3.2.1. The 2020–21 Event

As the most representative condition, the 2020–21 winter was the intersection of La Niña and a cold-PDO, spanning November 2020 to January 2021 (Figure 2). As expected, positive NDJ ΔP_{CR} was +8.46 and +8.04 mm day^{-1} for IMERG and CHIRPS, respectively (Table 1). This increase in precipitation was 74–102% greater than the NDJ climatology (Figure 7a,b). This condition was similar to the wintertime composite observed when La Niña coincided with the negative phase of the PDO (Figure 8b). Precipitation-inferred increases in riverine nutrient outflows into the NLC are potentially associated with monthly anomalies of Chl-a concentration in the NLC (ΔChl-a), reaching +0.28 mg m^{-3} during NDJ 2020–21 (Figure 7c) and +0.42 mg m^{-3} in December 2020 (Figure 9f).

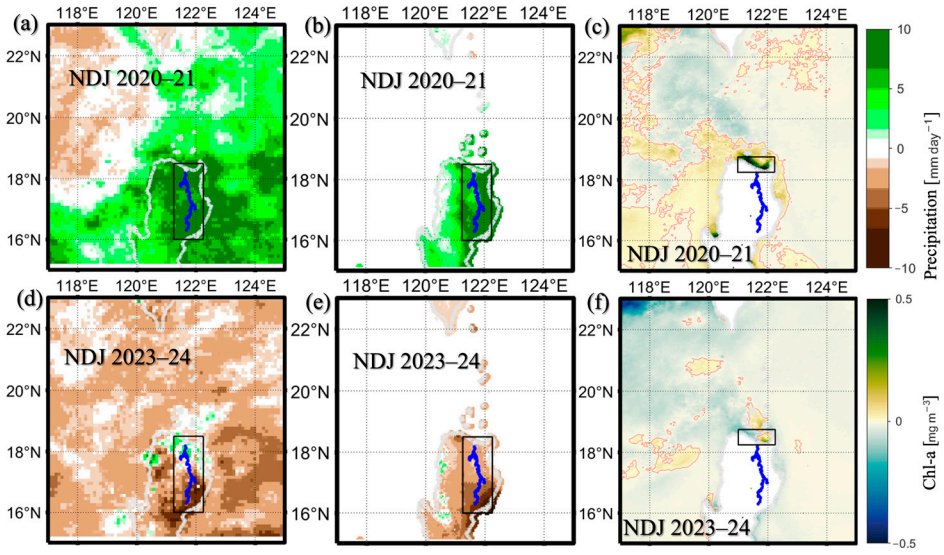


Figure 7. The precipitation anomalies (unit: mm day^{-1}) relative to their climatology during November to the next January (NDJ) in (**a**,**b**) 2020–21 (IMERG and CHIRPS), and (**d**,**e**) 2023–24 (IMERG and CHIRPS). The Chl-a anomalies (unit: mg m^{-3}) relative to the climatology during NDJ in (**c**) 2020–21

and (**f**) 2023–24. The temporal ranges for corresponding data are shown in Table 1. The black solid box indicates the spatial domain of the NLC.

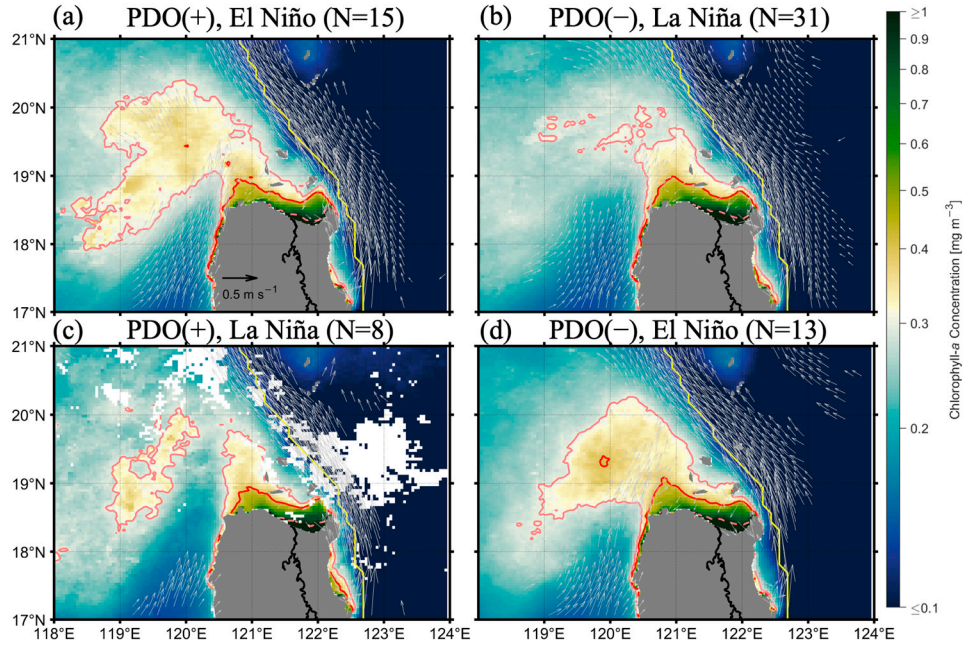
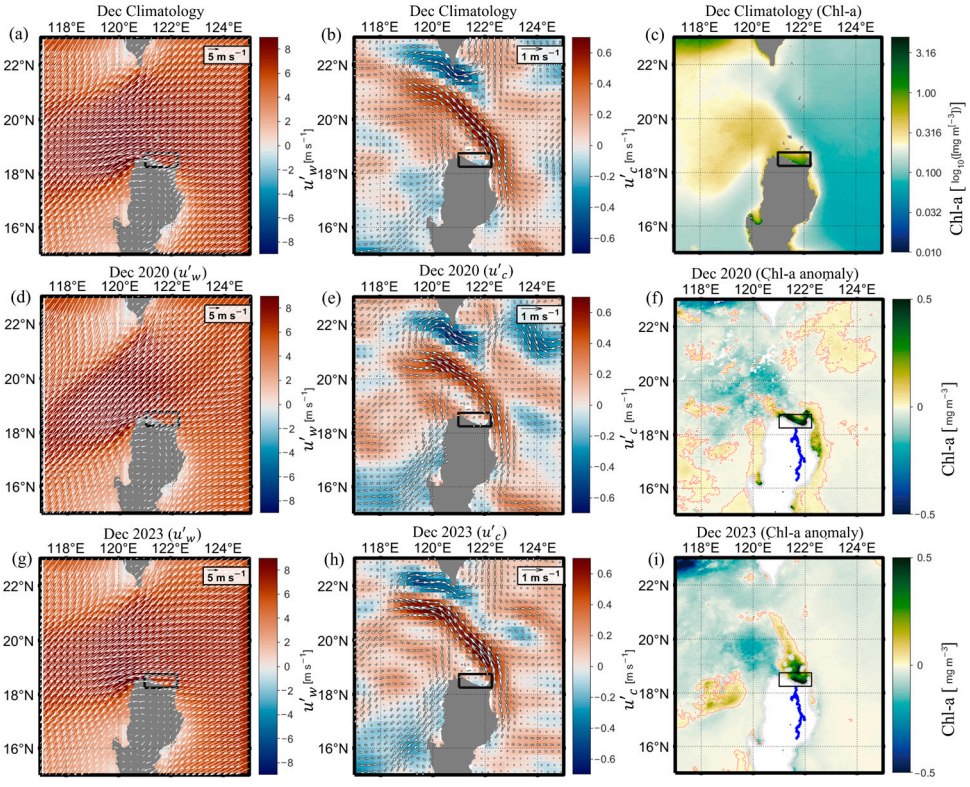


Figure 8. The NDJ composites of GlobColour Chl-a (color; unit: mg m^{-3}) and ADT-derived geostrophic currents (gray vectors; unit: m s^{-1}) from 1998 to 2024 when the climate background was (**a**) El Niño and positive PDO, (**b**) La Niña and negative PDO, (**c**) La Niña and positive PDO, and (**d**) El Niño and negative PDO. N represents the number of months included in each composite category. Only significant grids of shading colors and vectors are shown. Pink dashed, red solid, and pink solid lines represent contours of the GlobColour Chl-a values 1, 0.4, and 0.3 mg m^{-3}, respectively. Yellow lines denote the Kuroshio main axis in December during 1998–2024.



https://doi.org/10.3390/rs18234141

Figure 9. The monthly averaged u'_w (shaded color) and their vectors (white arrows) in (**a**) December 1993–2024, (**d**) December 2020, and (**g**) December 2023 (unit: m s^{-1}). The monthly averaged u'_c (shaded color) and their vectors (white arrows) in (**b**) December 1993–2024, (**e**) December 2020, and (**h**) December 2023 (unit: m s^{-1}) based on the Global Total dataset. The (**c**) monthly Chl-a December climatology (shaded color) and monthly Chl-a anomalies (shaded color) in (**f**) December 2020 and (**i**) December 2023 (unit: mg m^{-3}). Red contours in (**f**,**i**) represent the 0-level. The black solid box indicates the spatial domain of the NLC.

3.2.2. The 2023–24 Event

As a persistent cold-phase PDO continued to develop into the 2023–24 winter since March 2020, the El Niño mainly spanned from November 2023 to January 2024 (Figure 2). This established a destructive interference pattern that weakened the remote El Niño dry forcing originating in the tropics [29]. The suppression of the WNPAC thereby allowed the northeast winter monsoon to operate near normal intensity [45]. This atmospheric configuration modulated an inferred dual-source nutrient enrichment mechanism, including sustained hydrological discharge and wind-driven local upwelling [6]. The northeast monsoon, coupled with the complex topography of the Sierra Madre and Cordillera Central Mountain ranges [24], delivers stable and continuous precipitation over the CR basin. This resulted in a negative ΔP_{CR} of −3.21 mm day^{-1} during NDJ 2023–24, based on CHIRPS data (Figure 7e). However, the IMERG product shows that negative ΔP_{CR} decreased in magnitude to −2.22 mm day^{-1} during NDJ 2023–24 (Figure 7d). Although ΔP_{CR} was 37–57% below climatology, this moderate absolute reduction (~2–3 mm day^{-1}) left enough residual rainfall under the cold-PDO buffer to prevent severe drying of the CR. Therefore, near-normal riverine runoff into the NLC region is inferred (Table 1). This inference aligns with stable satellite-observed NDJ ΔChl-a in the NLC (−0.04 mg m^{-3}; Figure 7f), only 6% below the NDJ climatology (Table 1).

Concurrently, the uninhibited winter northeast monsoon winds drove a strong, positive WSC off northern and northwestern Luzon [3]. As demonstrated by previous studies [3,58], local positive WSC is the primary dynamical driver for the formation of the low NWL-SLA. This positive curl induced strong upward Ekman pumping and vertical mixing, which effectively increased the mixed-layer depth near the coast from northern to northwestern Luzon [3,59,60]. This physical upwelling pumped cold, nutrient-rich subsurface waters into the euphotic zone of the NLC, characterized by low SLA in December (Figure 10a), providing a massive, continuous supply of deep-sea nutrients [59].

The synergistic coupling of an inferred continuous riverine nutrient stream from the CR (sustained climatological buffering) and positive WSC-induced upwelling (subsurface nutrient pump) potentially provided a steady, multi-source nutrient supply to the coastal ocean (Figure 11c). This enrichment supported a highly productive, spatially extensive, and prolonged phytoplankton bloom, reaching a +0.37 mg m^{-3} ΔChl-a in December 2023 (Table 1). This condition was similar to the composite observed when El Niño coincided with the negative phase of the PDO (Figure 8d).

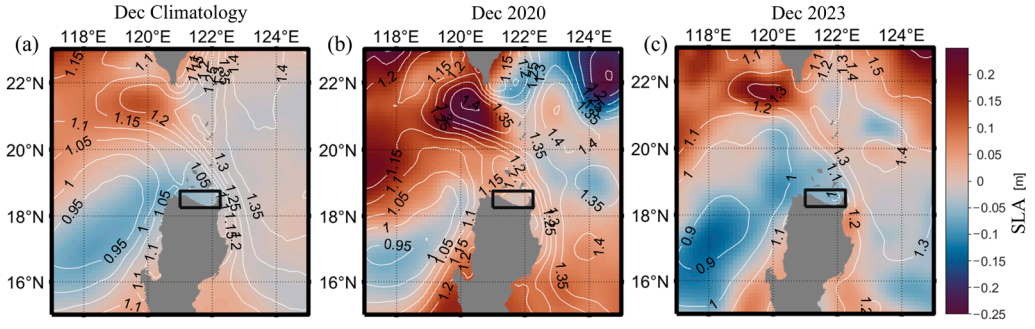


Figure 10. The monthly averaged SLA (shaded color) and ADT (white contours) in (**a**) December climatology during 1993–2024, (**b**) December 2020, and (**c**) December 2023 (unit: m). Elevated SLA in December 2020 reflects weakened KI, whereas the pronounced low NWL-SLA in December 2023 indicates enhanced upwelling and a steeper cross-strait gradient favoring stronger KI. The black solid box indicates the spatial domain of the NLC.

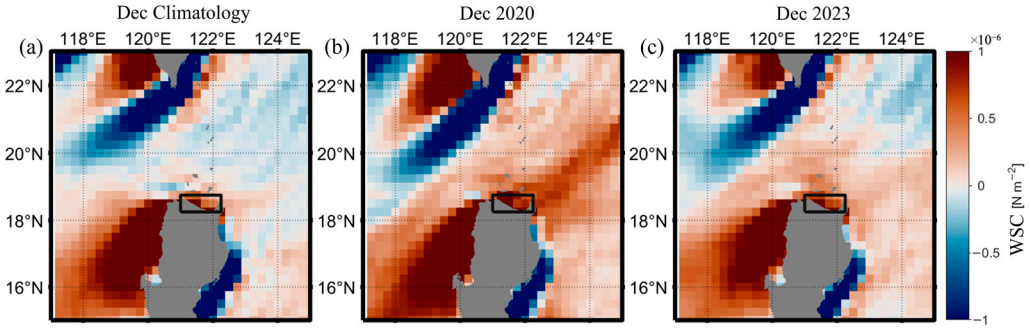


Figure 11. The monthly WSC (shaded color) in (**a**) December climatology during 1993–2024, (**b**) December 2020, and (**c**) December 2023 (unit: N m^{-2}). Persistent positive WSC off northern and northwestern Luzon demonstrates sustained Ekman pumping during both winters, maintaining subsurface nutrient upwelling even under the 2023–24 El Niño. The black solid box indicates the spatial domain of the NLC.

4. Discussion

4.1. Kuroshio Intrusion and Anomalous Winds

ENSO phase transitions not only alter terrestrial nutrient supplies via P_{CR} variability but also modulate the strength of the oligotrophic KI, which in turn controls the dispersion of Chl-a from the NLC westward to the northeastern SCS (Figure 1b). Although KI in December 2023 was generally suppressed compared to canonical El Niño events due to the cold-PDO background (Figures 9h and 10c), it remained stronger than La Niña-associated KI in December 2020 (Figures 9e and 10b). This KI produces a meridionally oriented band of Chl-a with a slight westward deflection (Figure 9i), which can be interpreted as a stream-like feature of oligotrophic water along the Kuroshio-induced Chl-a front [23] in the Luzon Strait (LSF-Chl-a). Notably, this LSF-Chl-a originated from the positive ΔChl-a in December 2023, which was mainly driven by positive WSC-induced upwelling (Figure 11c).

Notably, the northeast monsoon over the NLC was stronger in December 2020 (Figures 9d and 11b) than in December 2023 (Figure 9g). These also reflect the wintertime composites of La Niña (Figure 12b) and El Niño (Figure 12d) events during the cold-PDO. The KI-induced offshore advection in December 2023 in the rotated coordinate system with the θ_c =162° (Figures 9h and 10c) caused a banded Chl-a dispersion slightly deflected toward the northern SCS (Figure 9i) with the weaker northeast monsoon (Figure 9g). In contrast, the reduced offshore advection in December 2020 minimized the dispersion toward the northern SCS on the rotated coordinate system with the same θ_c (Figures 9e and 10b), effectively leaving the continuous river-supplied nutrients within the NLC (Figure 9f). Weaker KI during winter 2020–21 (Figure 9e) was compounded by increased river-induced nutrient inputs and the stronger northeast monsoon (Figure 9d). This explains why more Chl-a remained near the coast during NDJ 2020–21 than during NDJ 2023–24, even though single-month ΔChl-a was comparable in December.

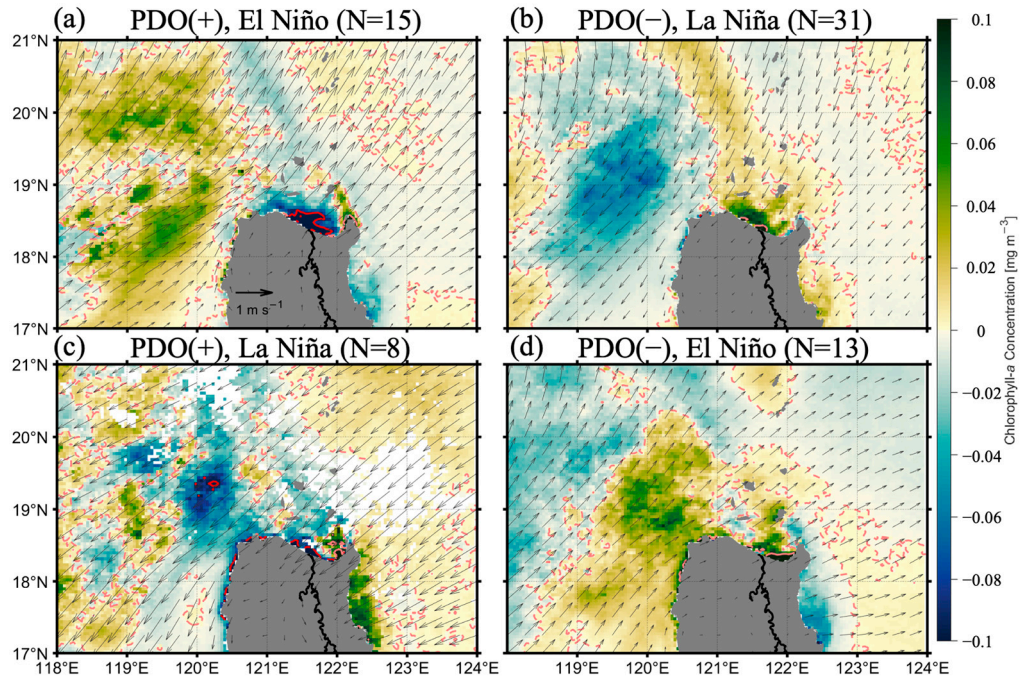


Figure 12. Anomalies of the NDJ composites of GlobColour Chl-a (color; unit: mg m^{-3}) and ERA5 winds (black vectors; unit: m s^{-1}) from 1998 to 2024 when the climate background was (**a**) El Niño and positive PDO, (**b**) La Niña and negative PDO, (**c**) La Niña and positive PDO, and (**d**) El Niño and negative PDO. N represents the number of months included in each composite category. Only significant grids of shading colors and vectors are shown. Pink dashed, red solid, and pink solid lines represent contours of the GlobColour Chl-a values 0.1, 0, and −0.1 mg m^{-3}, respectively.

4.2. Quantitative Attribution of NLC ΔChl-a

To quantify the relative contributions of the aforementioned atmospheric and oceanic mechanisms to the biogeochemical responses, statistical assessments were conducted beginning in the first available years for SeaWiFS (r97), MERIS (r03), and the early 2020s (r_{20}), as shown in Table 2. Based on a 3-month running average, a correlation analysis reveals a robust positive relationship between CHIRPS ΔP_{CR} and NLC ΔChl-a (r_{97} = 0.44, r_{03} = 0.44, and r_{20} = 0.64), confirming that precipitation-driven terrestrial runoff is a primary driver of nutrient enrichment. Furthermore, NLC ΔChl-a exhibits a significant positive correlation with the NLC WSC anomaly (r_{97} = 0.61, r_{03} = 0.63, and r_{20} = 0.63), reflecting the contribution of Ekman pumping. Conversely, a negative correlation between NLC ΔChl-a and the mean u'_c in the LS (KI intensity) is observed (r_{97} = −0.11, r_{03} = −0.15, and r_{20} = −0.15). This quantitative attribution supports the proposed "ENSO-dominated, PDO-modulated" causal chain, especially in the early 2020s, in which NLC ΔChl-a is dominated by ΔP_{CR} and WSC anomaly via precipitation-inferred and upwelled nutrients and modulated by KI intensity through offshore advection.

Table 2. Correlation coefficients between the NLC ΔChl-a and the corresponding primary atmospheric and oceanic drivers, including the CHIRPS ΔP_{CR}, WSC anomaly in the NLC, and the mean u'_c in the LS (KI intensity) in periods from September 1997 to 2024 (r_{97}), from 2003 to 2024 (r_{03}), and during the early 2020s (r_{20}). Their corresponding *p*-values are also included.

	r_{97}	r_{03}	r_{20}
ΔP_{CR}	+0.44 ($p < 0.01$)	+0.44 ($p < 0.01$)	+0.64 ($p < 0.01$)
WSC anomaly	+0.61 ($p < 0.01$)	+0.63 ($p < 0.01$)	+0.63 ($p < 0.01$)
KI intensity	−0.11 ($p = 0.057$)	−0.15 ($p = 0.015$)	−0.15 ($p = 0.255$)

5. Conclusions

In conclusion, this study reveals that the offshore transport of coastal Chl-a from the NLC into the northern SCS basin is fundamentally regulated by KI-induced biophysical advection and dispersion. This lateral biophysical conveyor is driven by the wintertime sea-level gradient across the LS, acting in concert with localized upwelling driven by the positive WSC off northwestern Luzon [3,59,61]. By serving as an efficient horizontal conveyor of shelf-derived biogenic properties [62], this mechanism plays a vital role in modulating nutrient inventories, phytoplankton dynamics, and primary productivity in the oligotrophic northern SCS under compounding climate modulation by the ENSO and the PDO [10,19,29].

Specifically, our findings highlight ENSO-dominated, cold-PDO-modulated asymmetric biogeochemical responses in the southern LS. El Niño/La Niña dynamically establishes low/high SLA near the NLC, setting up the KI-favored/KI-suppressed environment and reducing/increasing P_{CR}. The distinct decadal phases of the PDO facilitated the wet 2020–21 La Niña and buffered the theoretically dry 2023–24 El Niño.

During the 2020–21 La Niña, which coincided with the cold-PDO, constructive atmospheric interference initially induced an exceptionally wet meteorological condition in NDJ 2020–21. This resulting substantial increase in riverine runoff likely transported large quantities of suspended sediments, wash load, and terrestrial nutrients directly into the NLC, promoting a phytoplankton bloom. This response was reflected in a positive ΔChl-a of +0.28 ± 0.22 mg m^{-3} during NDJ 2020–21.

In contrast, during the 2023–24 El Niño, which coincided with the cold-PDO, destructive interference in the atmosphere suppressed the remote El Niño-induced dry forcing originating in the tropics by weakening the WNPAC (Figure 6c,d). This suppression of the WNPAC allowed the wintertime northeast monsoon to operate near normal intensity. This atmospheric configuration modulated an inferred dual-source nutrient enrichment mechanism. First, relatively stable, persistent monsoonal rainfall provided a hydrological buffer over the CR basin, maintaining near-normal riverine runoff and steady terrestrial nutrient input into the NLC. Second, the sustained winter monsoon winds drove a strong local positive WSC, promoting upward Ekman pumping and vertical mixing that transported cold, nutrient-rich subsurface waters into the euphotic zone of the NLC. The synergistic coupling of this inferred sustained riverine nutrient stream and wind-driven subsurface upwelling likely supported a highly productive, spatially extensive, and prolonged phytoplankton bloom. This response was reflected in a positive ΔChl-a of +0.37 ± 0.38 mg m^{-3} in December 2023, despite a near-neutral seasonal mean ΔChl-a of −0.04 ± 0.10 mg m^{-3} during NDJ 2023–24.

Compared with +0.42 ± 0.22 ΔChl-a in December 2020, ΔChl-a in December 2023 likely reflected multiple processes, including the cold-PDO-relieved condition, WSC-induced Ekman pumping, and a slight El Niño-related intensification of the KI, despite the prevailing cold-PDO background. In addition, transient weather disturbances and precipitation variability affected the El Niño-induced drought in northern Luzon Island, and atmospheric variations influenced wind-driven upwelling near the NLC. This dual climate modulation and KI-related biophysical coupling occurs in coastal boundary zones where western boundary currents intersect low-sea-level estuaries. Discovering this interdisciplinary chain reaction highlights the critical need to integrate both oceanic dynamics and terrestrial hydrological forcing when projecting coastal biogeochemical responses.

Although high-resolution satellite altimetry and gap-free blended ocean color products provide a robust basin-scale perspective on these teleconnections, the lack of comprehensive in situ observations of river discharge and terrestrial nutrient fluxes in the CR basin remains an inherent limitation of this study. This limitation, together with the lack of direct water-column observations, restricts our ability to fully characterize

biogeochemical budgets, subsurface nutrient distributions, and transient submesoscale processes. Furthermore, although the L4 gap-free GlobColour product provides a robust basin-scale perspective, coastal Chl-a retrievals near the Cagayan River mouth may experience optical interference from suspended sediments [56,57] and colored dissolved organic matter (CDOM) during extreme flushing events. However, such potential overestimations do not negate the pronounced interannual differences and the macroscopic spatial dispersion patterns modulated by the KI. It is a widely recognized consensus that, like snowflakes, no two El Niño or La Niña events are identical. Future studies incorporating high-resolution coupled physical-biogeochemical models and localized field campaigns will be essential to further understand this complex system. Nevertheless, this research significantly advances our understanding of how the most recent decadal cold-PDO regime in the early 2020s can act as a climatological buffer or amplifier for interannual ENSO events, offering a crucial predictive framework for evaluating the resilience of coastal marine ecosystems under compounding climate forcing.

Author Contributions: Conceptualization, Y.-H.T.; methodology, Y.-H.T.; validation, Y.-H.T.; formal analysis, Y.-H.T.; resources, C.-R.H.; writing—original draft preparation, Y.-H.T.; writing—review and editing, C.-R.H., H.C., L.W., and Y.-H.T.; funding acquisition, C.-R.H.; All authors have read and agreed to the published version of the manuscript.

Funding: This research was funded by the National Science and Technology Council of Taiwan, grant number NSTC 115-2611-M-019-015.

Data Availability Statement: All data used in this study are publicly available.

Acknowledgments: The authors thank NASA, NOAA, CMEMS, ECMWF, and UCSB CHC for providing datasets. The authors also thank the editor and five anonymous reviewers for their constructive comments and suggestions, which greatly improved the quality and scientific rigor of this paper.

Conflicts of Interest: The authors declare no conflicts of interest.

References

1. Shang, S.; Li, L.; Li, J.; Li, Y.; Lin, G.; Sun, J. Phytoplankton bloom during the northeast monsoon in the Luzon Strait bordering the Kuroshio. *Remote Sens. Environ.* **2012**, *124*, 38–48.
2. Chang, Y.; Shih, Y.; Tsai, Y.; Lu, Y.; Liu, J.T.; Hsu, T.; Yang, J.; Wu, X.; Hung, C. Decreasing trend of Kuroshio intrusion and its effect on the chlorophyll-a concentration in the Luzon Strait, South China Sea. *GIScience Remote Sens.* **2022**, *59*, 633–647.
3. Chiang, T.L.; Hsin, Y.C.; Wu, C.R. Numerical study on genesis of wintertime low sea level anomaly off northwestern Luzon and dominant factor in super-ENSO-related changes. *Ocean Model.* **2026**, *205*, 102817.
4. Shaw, P.T.; Chao, S.Y.; Liu, K.K.; Pai, S.C.; Liu, C.T. Winter upwelling off Luzon in the northern South China Sea. *J. Geophys. Res. Oceans* **1996**, *101*, 16435–16448.
5. Qu, T. Upper-layer circulation in the South China Sea. *J. Phys. Oceanogr.* **2000**, *30*, 1450–1460.
6. Wang, J.; Tang, D.; Sui, Y. Winter phytoplankton bloom induced by subsurface upwelling and mixed layer entrainment southwest of Luzon Strait. *J. Mar. Syst.* **2010**, *83*, 141–149.
7. Tseng, Y.H.; Ho, C.R.; Zheng, Q.; Zheng, Z.W. Loop current west of the Luzon Strait triggered by Kuroshio cut-off events east of Taiwan Island. *J. Geophys. Res. Oceans* **2025**, *130*, e2024JC021572.
8. Duteil, O.; Oschlies, A.; Böning, C.W. Pacific Decadal Oscillation and recent oxygen decline in the eastern tropical Pacific Ocean. *Biogeosciences* **2018**, *15*, 7111–7126.
9. Lim, H.; Dunne, J.P.; Stock, C.A.; Ginoux, P.; John, J.G.; Krasting, J. Oceanic and atmospheric drivers of Post-El-Niño chlorophyll rebound in the Equatorial Pacific. *Geophys. Res. Lett.* **2022**, *49*, e2021GL096113.
10. Lui, H.; Chen, C.A.; Hou, W.; Liau, J.; Chou, W.; Wang, Y.; Wu, C.; Lee, J.; Hsin, Y.; Choi, Y. Intrusion of Kuroshio helps to diminish coastal hypoxia in the coast of northern South China Sea. *Front. Mar. Sci.* **2020**, *7*, 565952.

11. Chen, C.A.; Huang, T.; Wu, C.; Yang, H.; Guo, X. Variability of the nutrient stream near Kuroshio's origin. *Sci. Rep.* **2021**, *11*, 5080.
12. Li, W.; Shang, Y.; Li, C.; Xu, C.; Laws, E.A.; Liu, X.; Huang, B. A stronger Kuroshio intrusion leads to higher chlorophyll a concentration in the northern South China Sea. *J. Geophys. Res. Oceans* **2025**, *130*, e2024JC021389.
13. Wang, L.; Wu, C.; Qiu, B. Modulation of Rossby waves on the Pacific North Equatorial Current bifurcation associated with the 1976 climate regime shift. *J. Geophys. Res. Oceans* **2014**, *119*, 6669–6679.
14. Sheremet, V.A. Hysteresis of a western boundary current leaping across a gap. *J. Phys. Oceanogr.* **2001**, *31*, 1247–1259.
15. Liu, K.; Chao, S.; Shaw, P.; Gong, G.; Chen, C.; Tang, T. Monsoon-forced chlorophyll distribution and primary production in the South China Sea: Observations and a numerical study. *Deep Sea Res. Part I Oceanogr. Res. Pap.* **2002**, *49*, 1387–1412.
16. Qu, T.; Kim, Y.Y.; Yaremchuk, M.; Tozuka, T.; Ishida, A.; Yamagata, T. Can Luzon Strait Transport play a role in conveying the impact of ENSO to the South China Sea? *J. Clim.* **2004**, *17*, 3644–3657.
17. Peñaflor, E.L.; Villanoy, C.L.; Liu, C.T.; David, L.T. Detection of monsoonal phytoplankton blooms in Luzon Strait with MODIS data. *Remote Sens. Environ.* **2007**, *109*, 443–450.
18. Nan, F.; Xue, H.J.; Chai, F.; Shi, L.; Shi, M.C.; Guo, P.F. Identification of different types of Kuroshio intrusion into the South China Sea. *Ocean Dyn.* **2011**, *61*, 1291–1304.
19. Wu, C.R. Interannual modulation of the Pacific Decadal Oscillation (PDO) on the low-latitude western North Pacific. *Prog. Oceanogr.* **2013**, *110*, 49–58.
20. Yu, K.; Qu, T. Imprint of the Pacific decadal oscillation on the South China Sea throughflow variability. *J. Clim.* **2013**, *26*, 9797–9805.
21. Yu, Y.; Xing, X.; Liu, H.; Yuan, Y.; Wang, Y.; Chai, F. The variability of chlorophyll-a and its relationship with dynamic factors in the basin of the South China Sea. *J. Mar. Syst.* **2019**, *200*, 103230.
22. Chen, C.A.; Wang, S.; Wang, B.; Pai, S. Nutrient budgets for the South China Sea basin. *Mar. Chem.* **2001**, *75*, 281–300.
23. Guo, L.; Xiu, P.; Chai, F.; Xue, H.; Wang, D.; Sun, J. Enhanced chlorophyll concentrations induced by Kuroshio intrusion fronts in the northern South China Sea. *Geophys. Res. Lett.* **2017**, *44*, 11565–11572.
24. Nippon Koei Co., Ltd.; Nikken Consultants, Inc. *The Feasibility Study of the Flood Control Project for the Lower Cagayan River in the Republic of the Philippines*; 4 Volumes; Japan International Cooperation Agency and Department of Public Works and Highways: Manila, Philippines, 2002. Available online: https://openjicareport.jica.go.jp/pdf/11871175.pdf (accessed on 4 September 2026).
25. Wu, X.; Mao, J. Interdecadal modulation of ENSO-related spring rainfall over South China by the Pacific Decadal Oscillation. *Clim. Dyn.* **2016**, *47*, 3203–3220.
26. Wang, B.; Zhang, Q. Pacific–East Asian teleconnection. Part II: How the Philippine Sea anomalous anticyclone is established during El Niño development. *J. Clim.* **2002**, *15*, 3252–3265.
27. Kubota, H.; Wang, B. How much do tropical cyclones affect seasonal and interannual rainfall variability over the western North Pacific? *J. Clim.* **2009**, *22*, 5495–5510.
28. Wang, X.; Liu, H. PDO modulation of ENSO effect on tropical cyclone rapid intensification in the western North Pacific. *Clim. Dyn.* **2016**, *46*, 15–28.
29. Gao, R.; Zhang, R.; Wen, M.; Li, T. Interdecadal changes in the asymmetric impacts of ENSO on wintertime rainfall over China and atmospheric circulations over western North Pacific. *Clim. Dyn.* **2019**, *52*, 7525–7536.
30. Lyon, B.; Camargo, S.J. The seasonally-varying influence of ENSO on rainfall and tropical cyclone activity in the Philippines. *Clim. Dyn.* **2009**, *32*, 125–141.
31. Villafuerte, M.Q., II; Matsumoto, J.; Akasaka, I.; Takahashi, H.G.; Kubota, H.; Cinco, T.A. Long-term trends and variability of rainfall extremes in the Philippines. *Atmos. Res.* **2014**, *137*, 1–13.
32. Bagtasa, G. Contribution of tropical cyclones to rainfall in the Philippines. *J. Clim.* **2017**, *30*, 3621–3633.
33. Hilario, M.R.A.; Olaguera, L.M.; Narisma, G.T.; Matsumoto, J. Diurnal characteristics of summer precipitation over Luzon Island, Philippines. *Asia-Pac. J. Atmos. Sci.* **2021**, *57*, 573–585.
34. Lee, C.A.; Huang, W.R.; Chang, Y.H.; Huang, S.M. Impact of multiple-scale circulation interactions on the spring diurnal precipitation over Luzon. *Sci. Rep.* **2021**, *11*, 9937.
35. David, C.P.; Custado, M.J.; Sekhon, N.; Ibarra, D.E. Forecasting tropical ENSO-induced drought conditions using sea surface height in the Western Pacific. *All Earth* **2022**, *34*, 55–65.
36. Xiang, Y.; Wang, T.; Wang, H.; Xu, H. Influence of the Pacific decadal oscillation on winter temperatures and precipitation over the southern Tibetan plateau. *J. Geophys. Res. Atmos.* **2024**, *129*, e2023JD038653.

37. Sun, B.; Li, H.; Wang, H.; Ding, Y.; Watanabe, M.; Ahn, J.B.; Takaya, Y.; Liu, Y.; Qiao, S.; Huang, Y. Impact of ENSO on Meiyu-Baiu-Changma rains: Processes, mechanisms, modeling, and future challenges. *Rev. Geophys.* **2026**, *64*, e2025RG000890.
38. Gershunov, A.; Barnett, T.P. Interdecadal modulation of ENSO teleconnections. *Bull. Am. Meteorol. Soc.* **1998**, *79*, 2715–2725.
39. Moron, V.; Lucero, A.; Hilario, F.; Lyon, B.; Robertson, A.W.; DeWitt, D. Spatio-temporal variability and predictability of summer monsoon onset over the Philippines. *Clim. Dyn.* **2009**, *33*, 1159–1177.
40. Sutton, W.R.; Srivastava, J.P.; Rosegrant, M.; Valmonte-Santos, R.; Ashwill, M. *Striking a Balance: Managing El Niño and La Niña in Philippines' Agriculture*; Report No. 132067; World Bank: Washington, DC, USA, 2019. https://doi.org/10.1596/31521.
41. Qian, J.H.; Robertson, A.W.; Moron, V. Diurnal cycle in different weather regimes and rainfall variability over Borneo associated with ENSO. *J. Clim.* **2013**, *26*, 1772–1790.
42. Rauniyar, S.P.; Walsh, K.J. Influence of ENSO on the diurnal cycle of rainfall over the Maritime Continent and Australia. *J. Clim.* **2013**, *26*, 1304–1321.
43. Huang, W.R.; Chang, Y.H.; Huang, P.H. Relationship between the interannual variations of summer convective afternoon rainfall activity in Taiwan and SSTA (Niño3.4) during 1961–2012: Characteristics and mechanisms. *Sci. Rep.* **2019**, *9*, 9378.
44. Huang, W.R.; Chien, Y.T.; Cheng, C.T.; Hsu, H.H.; Koralegedara, S.B. The role of sea surface temperature in shaping the characteristics of future convective afternoon rainfall in Taiwan. *npj Clim. Atmos. Sci.* **2023**, *6*, 198.
45. Lee, C.A.; Huang, W.R. Spring diurnal precipitation over Luzon Island: Interannual variability and underlying mechanisms. *J. Hydrometeorol.* **2026**, *27*, 581–595.
46. Lenssen, N.J.; Goddard, L.; Mason, S. Seasonal forecast skill of ENSO teleconnection maps. *Weather Forecast.* **2020**, *35*, 2387–2406.
47. Olaguera, L.M.; Matsumoto, J.; Kubota, H.; Inoue, T.; Cayanan, E.O.; Hilario, F.D. Interdecadal shifts in the winter monsoon rainfall of the Philippines. *Atmosphere* **2018**, *9*, 464.
48. Park, C.K.; Park, D.S.R.; Ho, C.H.; Park, T.W.; Kim, J.; Jeong, S.; Kim, B.M. A dipole mode of spring precipitation between southern China and Southeast Asia associated with the eastern and central Pacific types of ENSO. *J. Clim.* **2020**, *33*, 10097–10111.
49. Ragunjan, A.B.R.; De Jesus, M.A.; Domingo, S.A. Analysis of southwest monsoon rainfall and high precipitation events in Luzon Philippines. In *Proceedings of the OCEANS 2024*; IEEE: Singapore, 2024; pp. 1–7.
50. Li, Y.B.; Tam, C.Y.; Huang, W.R.; Cheung, K.K.; Gao, Z. Evaluating the impacts of cumulus, land surface and ocean surface schemes on summertime rainfall simulations over East-to-southeast Asia and the western north Pacific by RegCM4. *Clim. Dyn.* **2016**, *46*, 2487–2505.
51. Sohn, S.J.; Kim, W. Toward a better multi-model ensemble prediction of East Asian and Australasian precipitation during non-mature ENSO seasons. *Sci. Rep.* **2020**, *10*, 20289.
52. Nguyen–Le, D. Projected ENSO teleconnection on the Southeast Asian climate under global warming. *Environ. Res. Lett.* **2024**, *19*, 014001.
53. Mantua, N.J.; Hare, S.R.; Zhang, Y.; Wallace, J.M.; Francis, R.C. A Pacific interdecadal climate oscillation with impacts on salmon production. *Bull. Am. Meteorol. Soc.* **1997**, *78*, 1069–1079.
54. Hou, X.; Long, D.; Hong, Y.; Xie, H. Seasonal to interannual variability of satellite-based precipitation estimates in the Pacific Ocean associated with ENSO from 1998 to 2014. *Remote Sens.* **2016**, *8*, 833.
55. Hilario, F.; de Guzman, R.; Ortega, D.; Hayman, P.; Alexander, B. El Niño Southern Oscillation in the Philippines: Impacts, forecasts, and risk management. *Philipp. J. Dev.* **2009**, *36*, 9.
56. Milliman, J.D.; Syvitski, J.P. Geomorphic/tectonic control of sediment discharge to the ocean: The importance of small mountainous rivers. *J. Geol.* **1992**, *100*, 525–544.
57. Milliman, J.D.; Farnsworth, K.L. *River Discharge to the Coastal Ocean: A Global Synthesis*; Cambridge University Press: Cambridge, UK, 2011.
58. Zhong, Y.; Zhou, M.; Waniek, J.J.; Zhou, L.; Zhang, Z. Seasonal variation of the surface Kuroshio intrusion into the South China Sea evidenced by satellite geostrophic streamlines. *J. Phys. Oceanogr.* **2021**, *51*, 2705–2718.
59. Li, Q.P.; Dong, Y.; Wang, Y. Phytoplankton dynamics driven by vertical nutrient fluxes during the spring inter-monsoon period in the northeastern South China Sea. *Biogeosciences* **2016**, *13*, 455–466.
60. Lao, Q.; Liu, S.; Wang, C.; Chen, F. Global warming weakens the ocean front and phytoplankton blooms in the Luzon Strait over the past 40 years. *J. Geophys. Res. Biogeosci.* **2023**, *128*, e2023JG007726.

61. Wu, C.R.; Hsin, Y.C. The forcing mechanism leading to the Kuroshio intrusion into the South China Sea. *J. Geophys. Res. Oceans* **2012**, *117*, C07015.
62. Du, C.; Liu, Z.; Dai, M.; Kao, S.J.; Cao, Z.; Zhang, Y.; Huang, T.; Wang, L.; Li, Y. Impact of the Kuroshio intrusion on the nutrient inventory in the upper northern South China Sea: Insights from an isopycnal mixing model. *Biogeosciences* **2013**, *10*, 6419–6432.

Disclaimer/Publisher's Note: The statements, opinions and data contained in all publications are solely those of the individual author(s) and contributor(s) and not of MDPI and/or the editor(s). MDPI and/or the editor(s) disclaim responsibility for any injury to people or property resulting from any ideas, methods, instructions or products referred to in the content.